Showcasing a novel gas sensing platform based on a highly porous, stretchable laser-induced graphene pattern by a group of researchers led by Prof. Huanyu Cheng at The Pennsylvania State University.

Novel gas sensing platform based on a stretchable laser-induced graphene pattern with self-heating capabilities

The novel gas sensing platform, based on a highly porous laser-induced graphene pattern with a selective metal coating, provides localized healing to characterize low-dimensional nanomaterials and mixed metal oxides. Taken together with the stretchable design layout, the resulting gas sensor with excellent gas-sensing performance and mechanical robustness can potentially deconvolute various gaseous components in a mixture, which opens new opportunities in epidermal electronic devices.

As featured in:

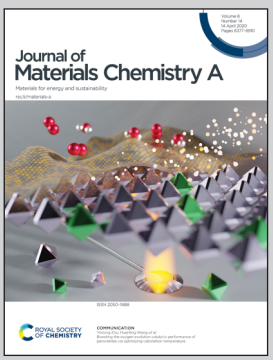

See Ning Yi, Huanyu Cheng *et al.*, *J. Mater. Chem. A*, 2020, **8**, 6487.

ROYAL SOCIETY OF CHEMISTRY

rsc.li/materials-a

Registered charity number: 207890

Journal of Materials Chemistry A

ROYAL SOCIETY OF CHEMISTRY

COMMUNICATION

View Article Online
View Journal | View Issue

Cite this: J. Mater. Chem. A, 2020, 8, 6487

Received 20th July 2019
Accepted 5th December 2019

DOI: 10.1039/c9ta07855j

rsc.li/materials-a

Novel gas sensing platform based on a stretchable laser-induced graphene pattern with self-heating capabilities†

Li Yang, ‡[ab] Ning Yi, ‡*[c] Jia Zhu, [b] Zheng Cheng,[dg] Xinyang Yin, [e] Xueyi Zhang, [e] Hongli Zhu [d] and Huanyu Cheng *[bcf]

Measurements of the gas sensing performance of nanomaterials typically involve the use of interdigitated electrodes (IDEs). A separate heater is often integrated to provide elevated temperature for improved sensing performance. However, the use of IDEs and separate heaters increases fabrication complexity. Here, a novel gas sensing platform based on a highly porous laser-induced graphene (LIG) pattern is reported. The LIG gas sensing platform consists of a sensing region and a serpentine interconnect region. A thin film of metal (*e.g.*, Ag) coated in the serpentine interconnect region significantly reduces its resistance, thereby providing a localized Joule healing in the sensing region (*i.e.*, self-heating) during typical measurements of chemoresistive gas sensors. Dispersing nanomaterials with different selectivity in the sensing region results in an array to potentially deconvolute various gaseous components in the mixture. The self-heating of the LIG gas sensing platform is first studied as a function of the applied voltage during resistance measurement and LIG geometric parameters (*e.g.*, linewidth from 120 to 240 μm) to achieve an operating temperature from 20 to 80 °C. Systematic investigations of various nanomaterials demonstrate the feasibility of the LIG gas sensing performance. Taken together with the stretchable design layout in the serpentine interconnect region to provide mechanical robustness over a tensile strain of 20%, the gas sensor with a significant response (6.6‰ ppm^{-1}), fast response/recovery processes, excellent selectivity, and an ultralow limit of detection (1.5 parts per billion) at a modest temperature from self-heating opens new opportunities in epidermal electronic devices.

Introduction

The recent development of wearable electronics has drawn considerable attention from both academia and industry. Because wearable electronic devices can conform to and follow the deformation of the skin, they are capable of capturing various essential mechanical,[1] thermal,[2] chemical,[3] electrical,[4] and biological signals,[5] demonstrating an excellent potential for future healthcare monitoring applications. Though continuous recording and analysis of gaseous compounds bear significant importance in healthcare, the study of wearable gas sensors for toxic gas detection,[6] environmental air quality monitoring,[7] and breath analysis[8] has only commenced recently. As one representative example, nitrogen dioxide (NO_2) is one of the most prominent toxic air pollutants from the combustion of fossil fuel. Inhaling at low concentration can cause symptoms such as asthma, bronchitis, and emphysema.[9,10] Long-term exposure can lead to heart failure and dysrhythmia.[11] Therefore, there is an increasing demand for the development of wearable gas sensors to provide accurate and continuous recording of NO_2. Wearable gas sensors can also enable the direct monitoring of the odours released from the human body to help inform the health conditions. Compared to their industrial counterparts, the development of wearable gas sensors needs to address additional challenging requirements, including lightweight and small form factor, low operating temperature, low energy consumption, and mechanical robustness upon various skin deformations.

Realizing the full potential to detect ultralow gas concentrations hinges on the effective use of nanomaterials because of their significantly increased surface to volume ratios. Previous studies of nanomaterials in the development of various gas sensors include metal oxide nanoparticles and nanowires,[12]

[a]Hebei Key Laboratory of Robot Perception and Human-robot Interaction, School of Mechanical Engineering, Hebei University of Technology, Tianjin 300401, China

[b]Department of Engineering Science and Mechanics, The Pennsylvania State University, University Park, PA, 16802, USA. E-mail: Huanyu.Cheng@psu.edu

[c]Department of Materials Science and Engineering, The Pennsylvania State University, University Park, PA, 16802, USA. E-mail: nzy5024@psu.edu

[d]Department of Mechanical and Industrial Engineering, Northeastern University, Boston, MA, 02115, USA

[e]Department of Chemical Engineering, The Pennsylvania State University, University Park, PA, 16802, USA

[f]State Key Laboratory of Digital Manufacturing Equipment and Technology, Huazhong University of Science and Technology, Wuhan, Hubei, 430074, China

[g]Plant Fiber Research Center, State Key Laboratory of Pulp and Paper Engineering, South China University of Technology, Guangzhou, Guangdong, 510640, China

† Electronic supplementary information (ESI) available: Experimental methods. See DOI: 10.1039/c9ta07855j

‡ These authors contribute equally.

quantum dot,[13] and two-dimensional (2D) materials such as graphene-based[14] and graphene-like layered nanomaterials.[15–17] Though graphene-based sensors exhibit high electrical conductivity, high mechanical strength, and low noise,[18–22] they are often associated with low sensitivity and poor selectivity.[16,17,23–26] Because of their rich active sites, selective molecular adsorption, semiconducting behaviours, and high yield preparation,[27–29] other graphene-like 2D materials such as molybdenum disulfide (MoS_2) have been explored as a promising material in the field of gas sensors. As the pristine MoS_2 has poor electrical conductivity, 3D MoS_2/graphene hybrid structures[30] or reduced graphene oxide (rGO)/MoS_2 composites[31] have been investigated to overcome the limitation. More importantly, the possible formation of the p–n junction between p-type rGO and n-type MoS_2 leads to enhanced sensitivity, selectivity, and signal-to-noise ratio (SNR) for the detection of target gas specious at an ultralow concentration.

Most of the highly sensitive gas sensors often suffer from a small response and slow response/recovery processes (or even no recovery) when operated at room temperature.[32–34] Elevated temperature from the integrated heating element is commonly used to expedite the desorption process of the adsorbed gas molecules. Though the heating elements can be conveniently fabricated with silicon (Si) micromachining technologies,[35,36] their performance suffers at high operating temperatures because of the instability from electromigration. The limited lifetime from chemical degradation[37] also hinders their practical use. In a separate effort, the use of metal nanowires (NWs) such as silver or copper has produced transparent heaters.[38,39] However, metal nanowires are prone to oxidation, leading to a degraded heating performance over time. Though gold (Au) coating can be used to prevent oxidation and improve biocompatibility, the increase in material costs poses a substantial obstacle for commercialization.[40] Additionally, the integration of a separate heating element complicates the fabrication process to construct a gas sensing system.

Among different configurations of gas sensors that explore field-effect transistor (FET),[41] surface work function (SWF),[42] and surface acoustic wave (SAW),[43] the ones based on the chemiresistor[44] are the most promising modality for the wearable gas sensors because of their simple design, relatively easy fabrication methods, and simplified data acquisition system from the straightforward measurement. Upon surface binding or adsorption of target gas molecules, the chemiresistor changes its electrical resistance due to the variation in the carrier concentration. Though simple in the design of the conventional chemiresistive sensor, noble metal or carbon-based interdigitated electrodes (IDEs) are still required to achieve an improved signal quality in the sensitive nanomaterials. However, the fabrication of IDEs often relies on a shadow mask deposition, screen printing, or inkjet printing. Because reducing the spacing between the fingers in IDEs increases the SNR of the resulting gas sensor, photolithographic processes are used to create the intricate IDEs designs, which complicates the fabrication process and increases the cost.

As a simple alternative to IDEs for integrating gas-sensitive nanomaterials, the highly porous laser-induced graphene (LIG) pattern[45–47] is systematically investigated as a novel gas sensing platform in this study. In a fast, cost-effective, and environmentally friendly process to fabricate the LIG, a transient CO_2 laser heating converts sp^3-hybridized carbon in the substrate such as polyimide into porous sp^2-hybridized carbon that is the carbon allotrope commonly found in graphene.[48] Though the LIG has been explored in numerous sensing applications,[49–52] the exploitation of the highly porous and p-type semiconducting LIG for gas sensing has seldom been reported until recently.[53] However, the LIG is only used as a gas sensing material to detect oxygen, nitrogen, and carbon dioxide. Additionally, the testing of the LIG and many other gas sensors was mostly carried out in a vacuum background rather than an ambient environment, posing a challenge for practical applications.

Leveraging the Joule heating or resistive heating (*i.e.*, self-heating) of the LIG as in the previous study,[53–55] we describe the approach to fabricate the LIG gas sensing platform with self-heating capabilities to characterize the gas sensing performance of various nanomaterials in this report. Eliminating the need for IDEs and separate heaters, the novel LIG gas sensing platform demonstrates its utility for characterizing various gas-sensitive nanomaterials (*e.g.*, MoS_2, rGO/MoS_2, or ZnO/CuO core/shell nanomaterials). Dispersing nanomaterials with different selectivity in the sensing region easily results in a high-density gas sensor array, which could potentially be used to deconvolute various gaseous components in the mixture relevant to the environmental or healthcare applications in the future studies. As a representative example to demonstrate the unique advantages of the LIG gas sensing platform, we systematically investigated the gas sensing performance of the LIG decorated with rGO/MoS_2 nanomaterials in various self-heating conditions. At a proper self-heating condition to 60 °C, the rGO/MoS_2-LIG gas sensor exhibits fast response/recovery and ultrasensitive detection of NO_2, with a limit of detection of 1.5 parts per billion (ppb) at low power. When designed in a stretchable pattern, the LIG gas sensing platform can withstand a uniaxial tensile strain of 20% that is comparable to the level of maximum deformation on the skin surface to open new opportunities for the epidermal electronic devices.

Results and discussion

The LIG gas sensing platform is designed to consist of a straight sensing region and a serpentine interconnect region where the wavy LIG pattern is coated with a thin metal (*e.g.*, Ag) layer. The self-heating of the LIG results from the Joule heating (or resistive heating) during the resistance measurement of the chemoresistive LIG gas sensors upon the externally applied voltage. As the thin metal layer coated on the wavy LIG significantly reduces the resistance in the serpentine interconnect region when compared to that of the sensing region, the Joule heating leads to localized heating in the LIG sensing region. The stretchable, highly porous LIG gas sensing platform is created by using a simple laser scribing process with a selective coating of metal layer in the serpentine interconnect region (Fig. 1a). In brief, computer-designed layouts of porous LIG patterns on

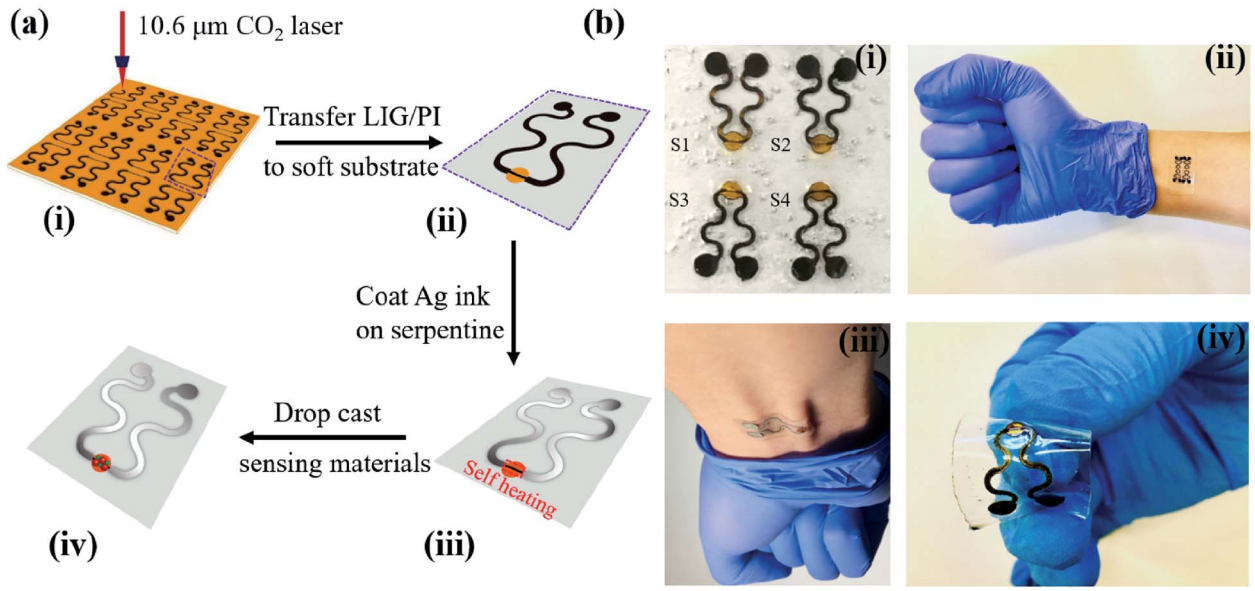

Fig. 1 Schematic illustration of the fabrication process and demonstration of the wearable gas sensing platform. (a) Schematic illustration of the steps to prepare the stretchable laser-induced graphene (LIG) gas sensing platform: (i) porous LIG pattern on a polyimide (PI) film created by a laser scribing process, (ii) LIG/PI pattern transferred onto a soft elastomeric substrate, (iii) serpentine regions coated with conductive metal such as the Ag ink, (iv) gas-sensitive nanomaterials drop cast at the sensing region. (b) Optical images of the LIG gas sensing platform and its demonstration to follow various deformations applied to it. Various sensitive nanomaterials dispersed at the LIG sensing region could be designed with high selectivity to detect a specific component or with different selectivity to various components in the gaseous mixture upon various self-heating conditions. Collectively, the sensing response from the sensor array enables combinatorial sensing of multiple gas components in the mixture. Images of (i) a representative sensing platform with four sensing units arranged in an array of two by two on a soft substrate, (ii) sensing platform that followed the skin deformation from holding the fist, and deformations of a single sensing unit (iii) on the human wrist and (iv) in bending.

polyimide (PI) films rapidly formed with high precision in an ambient environment by using a laser system (Fig. 1a(i)), with the remaining PI underneath the LIG to ensure its mechanical integrity. Transferring the LIG pattern onto a soft elastomeric substrate (Fig. 1a(ii)) was followed by drop casting Ag ink (Novacentrix AJ-191) in the serpentine interconnect region to yield a stretchable LIG gas sensing platform (Fig. 1a(iii)). As the Ag coating significantly reduces the resistance in the serpentine interconnect region to result in localized heating in the sensing region, the power consumption is minimized. While it is possible to separately fabricate the LIG sensing region and the Ag wavy serpentine interconnect region, the creation of the Ag pattern would involve more complicated fabrication processes. Additionally, the significantly reduced contact area and quality at the Ag/LIG interface would lead to poor mechanical robustness, especially upon mechanical perturbations such as various skin deformations. Drop-casting various highly sensitive nanomaterials (*e.g.*, rGO, MoS_2, rGO/MoS_2, or ZnO/CuO core/shell nanomaterials) in the LIG sensing region (Fig. 1a(iv)) of the individual gas sensor in the array completed the fabrication of the stretchable gas sensing platform. In a representative demonstration, four different sensing units (S1–S4) arranged in an array of two by two were prepared (Fig. 1b(i)). The array conformed to the wrist even upon the skin deformation from holding the fist (Fig. 1b(ii)). Each sensing unit is capable of bending to a cylinder (Fig. S1†) and following various deformations applied to it (Fig. 1b(iii and iv)).

The laser scribing process yielded continuous, porous LIG structures (Fig. 2a). Raman spectrum of the LIG (Fig. 2b) also exhibited the D peak (~1350 cm^{-1}), G peak (~1572 cm^{-1}), and 2D peak (~2697 cm^{-1}), with a relative large ratio of I_G/I_{2D} to indicate the presence of few-layered porous graphene, consistent with the literature reports.[56] The sensitive nanomaterial with high selectivity will be chosen to detect a specific gaseous component in the mixture. Collectively, the sensing response from different sensors in the high-density array enables deconvolution of multiple gaseous components in the mixture relevant to the healthcare or environmental applications. As the first step toward this goal, here in this study, we will first demonstrate the design rationale of the LIG gas sensing platform and systematic investigations of an ultrasensitive NO_2 gas sensor to highlight the feasibility of the LIG sensing platform. The design example of the NO_2 gas sensor includes the use of low-dimensional nanomaterials such as MoS_2 and rGO/MoS_2 with controlled surface morphologies. Considering the intrinsic p-type semiconducting LIG,[53] introducing n-type MoS_2 nanomaterials[57] on LIG could form p–n junctions to enhance the sensing performance.[58,59] In the next step, we will demonstrate the versatility of the LIG gas sensing platform by exploring it to characterize heterostructure metal oxides. As a representative heterostructure metal oxide, ZnO/CuO core/shell nanomaterials prepared by calcination of a Cu–Zn bimetallic metal–organic framework (MOF) will be explored. We will specifically focus on the selectivity of this class of nanomaterials, which will help

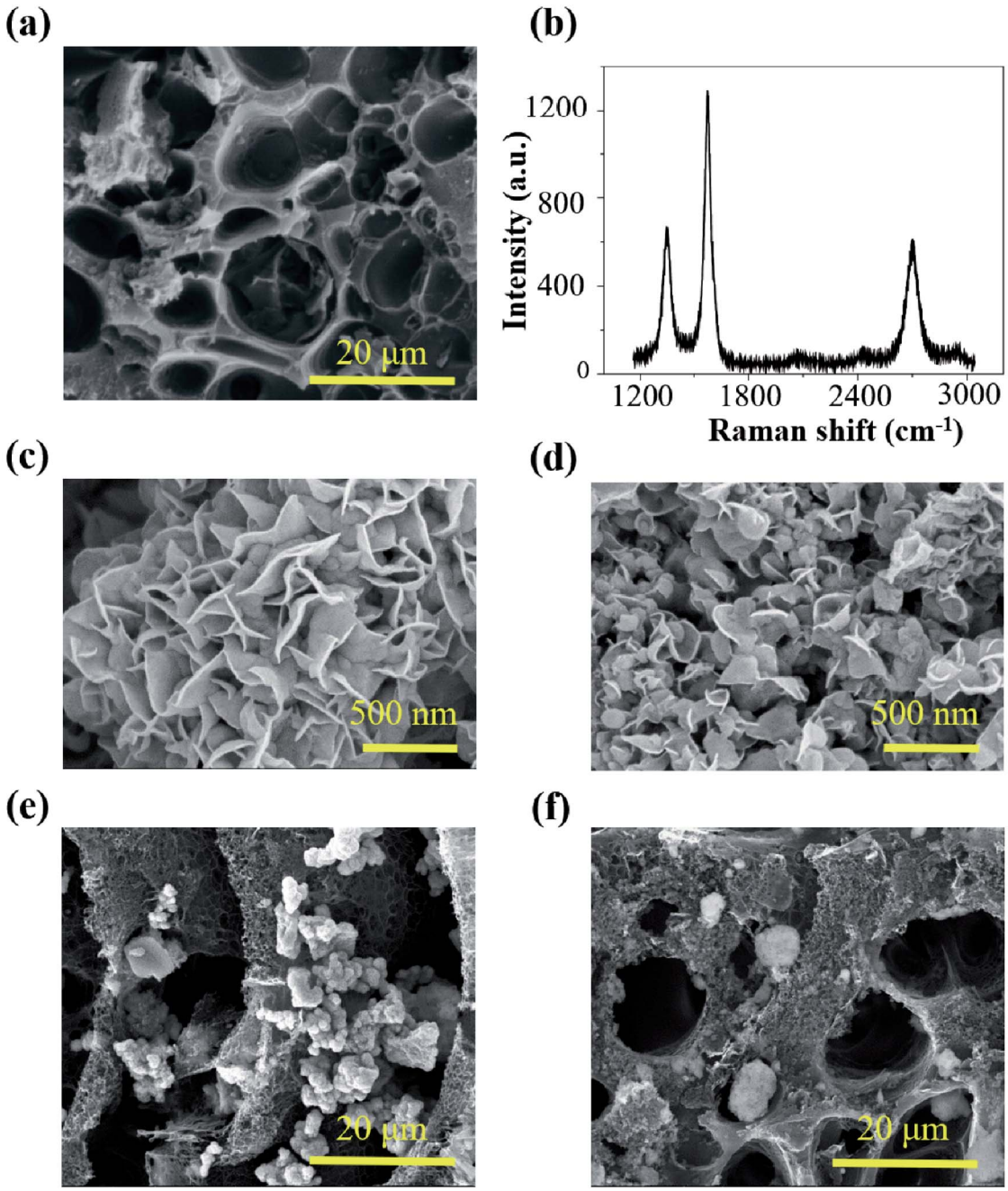

Fig. 2 Characterization of the LIG gas sensing platform. (a) Scanning Electron Microscope (SEM) image and (b) Raman spectrum of porous LIG electrode. SEM images of reduced graphene oxide/molybdenum disulfide (rGO/MoS_2) nanoflowers synthesized (c) without ("large petal") and (d) with ("small petal") the as-bought NaCl salt crystals. SEM images of rGO/MoS_2 nanoflowers with (e) "large petal" and (f) "small petal" structure dispersed on the porous LIG electrodes.

illustrate the feasibility to deconvolute the gaseous components in a mixture with the LIG gas sensing platform.

The preparation of the rGO/MoS_2 composite solution followed the previously reported procedure. In brief, as received NaCl crystal fillers were added to a mixture of precursors (*i.e.*, molybdenum oxide, thioacetamide, urea, and GO). The NaCl crystal fillers created the confined space among them, allowing the rGO/MoS_2 to synthesize only within such a confined space. The morphology of the rGO/MoS_2 was also regulated by the size of the confined space, as in the previous report.[60] In the following study, two different rGO/MoS_2 samples were synthesized without or with as-bought NaCl crystal fillers. As characterized by the scanning electron microscopy (SEM), the rGO/MoS_2 composites exhibit hierarchical flower-like structures consisting of a large number of petals (Fig. 2c and d). The resulting rGO/MoS_2 nanoflower is associated with large specific surface area, consistent with the previous literature report.[61] The rGO/MoS_2 nanoflower synthesized with as-bought NaCl

crystal fillers exhibit smaller sample size and higher specific surface area (Fig. 2d, "small petal") than that synthesized without salt (Fig. 2c, "big petal"). As the literature report[31] indicates an optimized gas sensing performance when the rGO concentration is over 0.5 mg ml^{-1} and the MoS_2 concentration is in the range from 0.64 to 1.28 mg ml^{-1}. A proper ratio of rGO to MoS_2 is also desired, because too much rGO will shield gas sorption sites on MoS_2 and too little rGO will reduce the conducting pathway. While the optimized rGO/MoS_2 ratio is not investigated in this study, both of the rGO/MoS_2 samples have a MoS_2 concentration of 1.33 mg ml^{-1} and an rGO concentration of 0.7 mg ml^{-1}, to be consistent with the above report. The rGO/MoS_2 composite solutions were then drop cast in the LIG sensing region to yield the stretchable gas sensor. The successful integration of rGO/MoS_2 nanoflowers on the porous LIG sensing region was confirmed by the SEM (Fig. 2e and f). The formed interconnected network has a small contact resistance, which is beneficial for gas sensing performance. The elemental compositions of the LIG gas sensors before and after dispersing rGO/MoS_2 were also examined by X-ray photoelectron spectra (XPS) (Fig. S2†). Ascribing the Si 2s, Si 2p, and O 1s peaks to the siloxane of the PDMS substrate, the survey spectrum of bare LIG samples (Fig. S2a†) indicates the presence of the LIG on PDMS. Compared with survey spectrum of bare LIG samples (Fig. S2a†), the survey spectrum of LIG with rGO/MoS_2 synthesized using NaCl crystals (Fig. S2b†) informs the presence of MoS_2 on the LIG. The characteristic features of MoS_2 have been observed: Mo 3d doublet centered at the binding energy of 232 eV and 228 eV (Fig. S2c†) and the S 2p peak centered at 162 eV (Fig. S2d†).[31] It should be noted that it is difficult to control and calculate the ratio of rGO/MoS_2 over LIG though the volume of the rGO/MoS_2 solution could be accurately controlled in drop casting.

Though room temperature gas sensors eliminated the adverse thermal effect, moderate heating in gas sensing materials (*e.g.*, graphene/MoS_2) would still be favourable to enable fast response/recovery and enhanced reversibility.[30] As the Joule heating of the LIG material itself has been reported,[53–55] we will first investigate the localized self-heating effect of the LIG gas sensing platform with a LIG sensing region and an Ag/LIG serpentine interconnect region. Different from the other gas sensors (even including LIG gas sensors) that integrate additional heaters,[54] the self-heating effect of the LIG gas sensing platform could be exploited to reduce the device complexity for characterizing various gas-sensitive nanomaterials.

The self-heating effect of the LIG gas sensing platform hinges on its geometric parameters and location-dependent conductivity (*i.e.*, Ag coated LIG in the serpentine interconnect region). A strong self-heating effect requires the resistance of the LIG sensing region to be significantly larger than that of the serpentine region. Similar to the conventional design of heaters, a smaller linewidth and a longer length in the LIG sensing region increased its relative resistance to the serpentine interconnect region. However, the Ag ink coating in the serpentine interconnect region drastically reduced its resistance, obviating the need for a significantly reduced linewidth and increased length in the LIG heating region. While the laser processing parameters change the sheet resistance of the LIG, the additional change in the linewidth and length of the LIG sensing region further provides ways to tune the resistance of the LIG sensing region. Given the same laser processing parameters, the resistance of the LIG sensing region was found to be proportional to its length (Fig. S3a†), yielding a sheet resistance of 78 Ω sq^{-1}. Though the resistance decreased as the width increased (Fig. S3a†), the inverse proportional relationship was not observed, because of the change in the sheet resistance (ranging from 110 Ω sq^{-1} to 60 Ω sq^{-1} with the increasing width from 150 μm to 292 μm) from creating the LIG pattern of different widths.

The transient Joule heating was characterized for the LIG sensing region with a length of 2.5 mm and width of 120 μm (an initial resistance of ~2.3 kΩ) (Fig. 4a). The peak temperature rapidly increased to equilibrium for an applied voltage in the range from 0.5 V to 12 V (Fig. 4a). The time to equilibrium of less than 20 s is much shorter than the other heaters based on graphene or nanowires of 50–300 s.[62–64] As the Joule heating induced temperature rise linearly scales with the input power applied on the LIG sensing region, a higher applied voltage in this range induced a higher temperature (Fig. S4†). The infrared thermal images of the LIG surface also confirmed the localized heating and temperature rise from Joule heating in the LIG sensing region due to its relatively high resistance in comparison with the Ag/LIG serpentine interconnect region (Fig. S5†). The temperature of the gas sensing region was controlled to 20.1 °C, 39.8 °C, 60.4 °C, and 80.1 °C, by applying a voltage of 0.5 V, 7 V, 10 V, and 12 V, respectively.

The steady-state characteristics of the LIG gas sensing platforms were analyzed by measuring their current–voltage (*I–V*) curves with different sizes in the LIG sensing region (Fig. 3b). In the *I–V* curve measurement, the voltage was ramped up from 0 V to 11 V in a step-wise manner (*i.e.*, step increase of 1 V per 20 s). Though the *I–V* curves were relatively linear despite the temperature rise from self-heating, there was still a small change in the resistance of the LIG gas sensing platform. Taking the LIG sensing region with a length of 2.5 mm and width of 120 μm as an example, its resistance was shown to decrease (Fig. 3c) because of the negative temperature coefficient in the graphitic materials.[65] However, the resistance reduction was small to be negligible, as the resistance of the LIG gas sensing platform only gradually decreased from 2.331 kΩ to 2.220 kΩ by 4.7% in the voltage range from 0 V to 11 V. By considering the small variation in the electrical resistance of the LIG gas sensing platform, an improved agreement was observed between the temperature rise and the input power (Fig. S3†). Because of the relatively stable resistance, the current in the LIG gas sensing platform was observed to ramp up in a stepwise manner from 0 mA to 5.44 mA (Fig. 3c).

The sensing mechanism of the chemiresistive gas sensor relies on the direct charge transfer between the target gas molecules (*e.g.*, NO_2) and sensitive nanomaterials (*e.g.*, MoS_2, rGO/MoS_2, or ZnO/CuO core/shell nanomaterials). In the rGO/MoS_2 nanoflowers, while the p-type rGO sheets provide the overall conductivity, the n-type MoS_2 on the rGO sheets has multiple active sites with selective affinity to NO_2 gas molecules

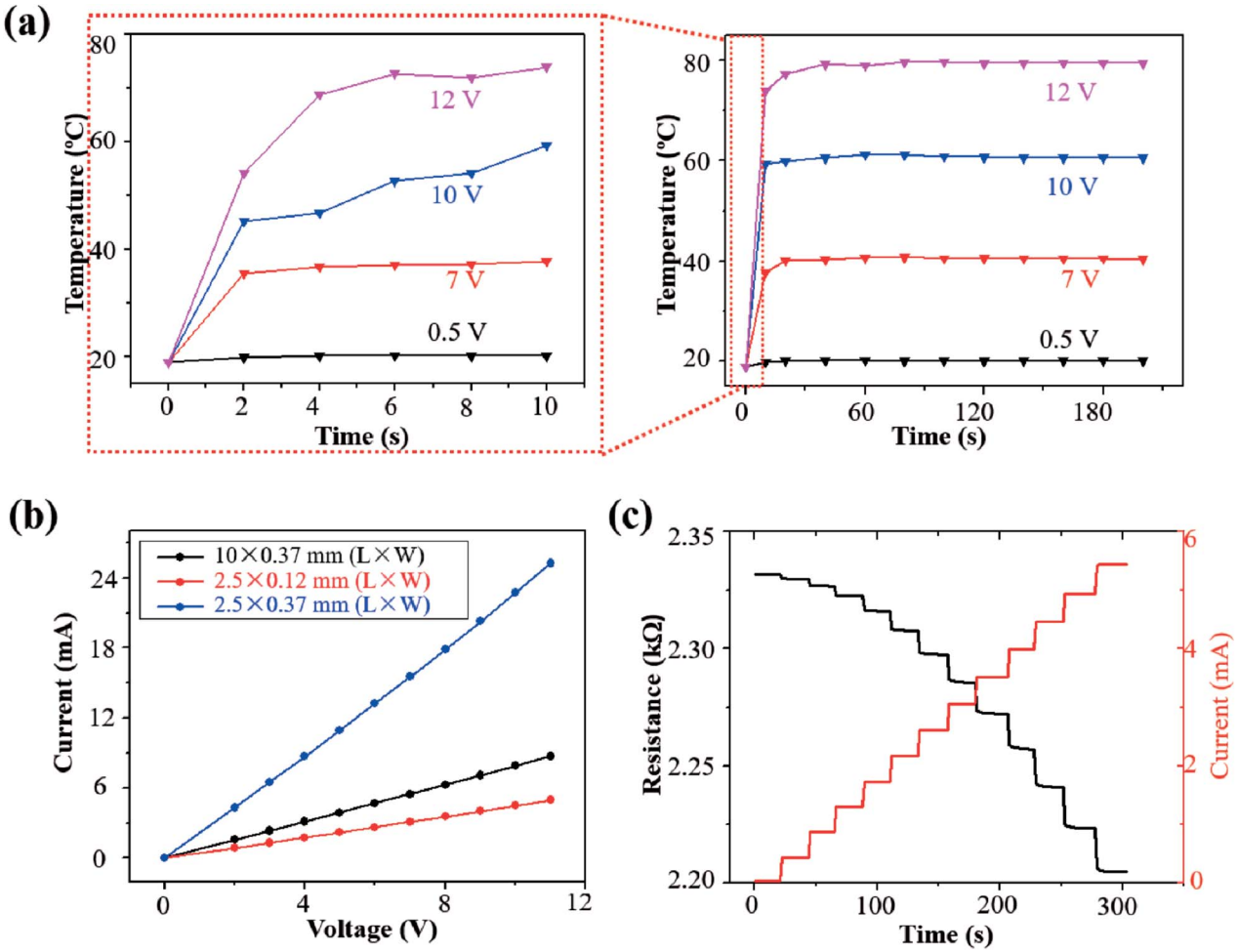

Fig. 3 Characterization of the LIG electrode with self-heating capabilities. (a) The time-dependent temperature profile of the LIG electrode when different input voltages were applied during the resistance measurement of the chemiresistor. The inset shows the zoom-in of the measurement in the first 10 s. (b) Current–voltage (I–V) curves of three LIG electrodes with different sizes. (c) The change in resistance of and current in the LIG electrode with a length of 2.5 mm and width of 120 μm as a function of the time.

for sensing. The adsorption of NO_2 on the surface of rGO/MoS_2 nanoflowers continuously withdrew electrons from rGO/MoS_2, which extended both of the electron depletion and hole accumulation regions at the interface of the p–n junction. The accumulation of holes increases the major carrier concentration of the gas sensor, thereby decreasing the overall resistance.

It should be pointed out that the carrier concentration of the LIG changes upon NO_2 adsorption is evidenced by its response to NO_2 gas molecules (Fig. S6†). The gas sensor response was defined as the ratio of its electrical resistance R in the presence of target gas to that R_0 in the air. The gas sensing response of pristine porous LIG sensing regions to NO_2 was observed to depend on the laser scribing parameters. When a power of 16% and a speed of 10% were used in the CO_2 laser scribing process, the resulting LIG sensing regions showed poor sensitivity (~0.3‰) and apparent baseline shift when exposed to 1 ppm NO_2 at 20 °C (Fig. S6a†). Reducing both the power and speed in the laser scribing process (power of 3% and speed of 0.8%) yielded pristine porous LIG sensing regions with significantly improved performance (*i.e.*, response of 12‰ and SNR of 434) (Fig. S6b†). It should be pointed out that the obtained SNR is significantly larger than those of the previous studies based on 2D material[66] due to the significantly reduced noise levels though the response may be small. Meanwhile, the excellent selectivity of the sensor to NO_2 over a wide range of other inferencing gas species (*e.g.*, acetone, ethanol, ammonia, SO_2, CO, and NO) was also confirmed (Fig. S6c†). In addition to the change in laser scribing parameters, dispersing highly sensitive materials such as MoS_2 (Fig. S7†) or rGO/MoS_2 (Fig. 4a) in the LIG sensing regions also improved the gas sensing performance to NO_2. For instance, the response of the porous LIG line (power of 16%, speed of 10%) coated with rGO/MoS_2 (or MoS_2) exhibited significant increase to 7‰ (or 5‰), corresponding to *ca.* 20-fold increase when compared to the pristine porous LIG sensing regions without nanomaterial coating. Upon NO_2 exposure of 6 min, a high SNR of 482 (or 285) was also observed in the LIG sensing region coated with rGO/MoS_2 (or MoS_2). Considering the vast difference between sensors with and without the highly sensitive nanomaterials, the response of the gas sensor should be mainly contributed by the nanomaterials,

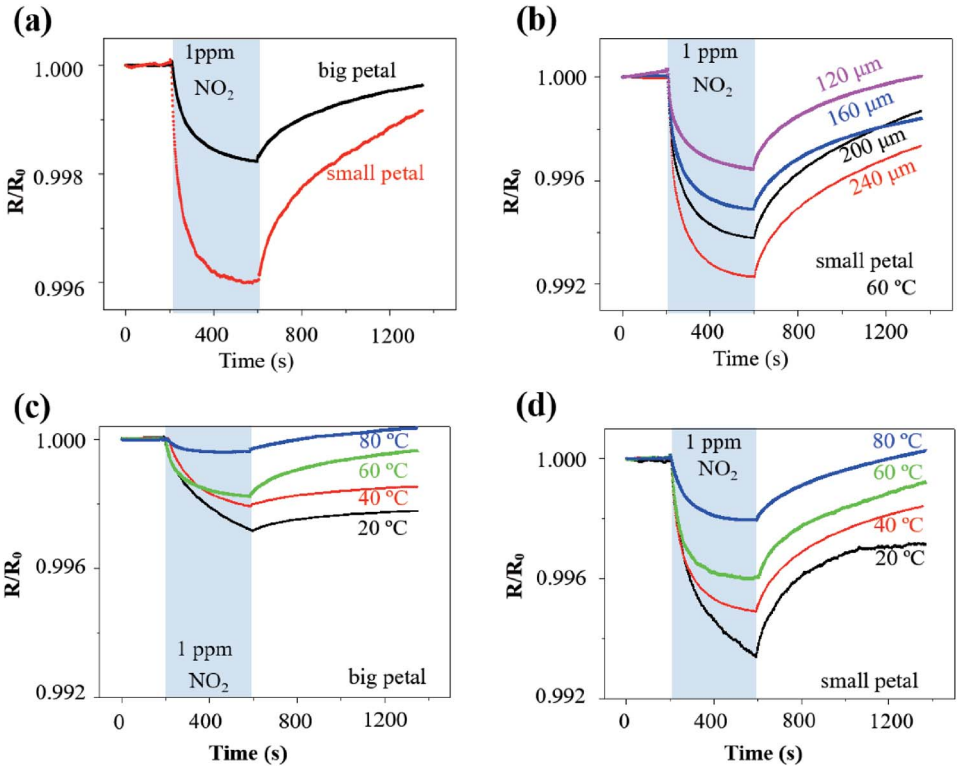

Fig. 4 Effects of the width and operating temperature from self-heating on the gas sensing performance. (a) The typical response curves of rGO/MoS_2 nanoflowers with the small petal and big petal structure on the LIG sensing platform at 60 °C to NO_2 of 1 ppm. (b) Time-dependent response curves of rGO/MoS_2 nanoflowers with the small petal on the LIG with various widths at 60 °C. (c) Sensor response of rGO/MoS_2 nanoflowers with the big petal to 1 ppm NO_2 at various temperatures from self-heating. (d) Sensor response of rGO/MoS_2 nanoflowers with the small petal to 1 ppm NO_2 at various temperatures from self-heating (ppm: parts per million; 1 ppm = 10^{-4}%).

which demonstrates that the LIG gas sensing platform enables the characterization of sensitive nanomaterials.

The rGO/MoS_2 nanoflowers with the small petal structure was selected to investigate the width effect on the gas sensor performance, because it demonstrated a more substantial response of 4.0‰ than that with the big petal structure of 1.8‰ to NO_2 of 1 ppm at 60 °C from self-heating (10 V applied on the LIG with a linewidth of 120 μm and length of 2.5 mm) (Fig. 4a). The more significant response in the LIG with the small petal structure than that with the big petal structure was also observed at other temperature values, *i.e.*, 6.6‰ *vs.* 2.8‰ at 20 °C, 5.1‰ *vs.* 2.0‰ at 40 °C, and 2.0‰ *vs.* 0.4‰ at 80 °C (Fig. S8†). The LIG with the small petal structure is associated with the reduced feature size and more uniform distribution of the nanomaterials. The increased specific surface area and the possibly formed p–n junction lead to a more substantial response and faster response/recovery processes. In contrast to the previous literature reports that the response/recovery processes have only been qualitatively described, we have introduced the angle of the plateau (defined as the tangent angle of the response/recovery curves at the end of adsorption/desorption) to quantitatively capture these processes. The smaller the angle of the plateau, the faster the response/recovery processes. With such a new definition, the response process in the LIG with the small petal structure (angle of the plateau of 2°) was indeed faster than that with the big petal structure (slope of the plateau of 3°).

Different voltage inputs were first applied to the LIG sensing region with various linewidths to ensure their temperatures remained the same such as at 60 °C. In particular, a voltage of 20 V, 15 V, 12 V, and 11 V was applied on the LIG with a linewidth of 120 μm, 160 μm, 200 μm, and 240 μm, all with the same length of 6 mm. Next, dispersing rGO/MoS_2 nanoflowers with small petal structure on the LIG sensing region with various linewidths prepared chemiresistive gas sensors. The electrical resistance of the resulting gas sensors decreased upon exposure to NO_2 of 1 ppm and recovered in the air due to the desorption of NO_2 (Fig. 4b). The magnitude of the response to NO_2 of 1 ppm at 60 °C increased from 3‰ to 8‰ as the linewidth of LIG sensing region increased from 120 μm to 240 μm (Fig. 4b). Consisting of the electrical resistance $R_{sensing}$ in the sensing region, $R_{serpentine}$ in the serpentine region, and the contact resistance $R_{contact}$ between nanomaterials (*e.g.*, rGO/MoS_2) and LIG, the total resistance R_{total} of the resulting gas sensor would be the sum of the three. Forming a parallel connection between the LIG and the nanomaterial such as rGO/MoS_2 would indicate a more significant response in the LIG with a smaller linewidth, which cannot explain the trend in the experiment. The increased response with the increasing linewidth could be likely attributed to the non-uniform temperature distribution in the

LIG sensing region (Fig. S4†). Consistent with the literature reports on ohmic microheaters,[67] non-uniform temperature distribution resulted in a lower temperature at the edge than that at the central region of the LIG sensing region. Because the rGO/MoS_2 sensing material showed a more substantial response at a lower temperature (Fig. 4c and d), the lower temperature at the edge region of the LIG sensing region with a larger linewidth gave rise to the more significant response. Additionally, the incomplete recovery to NO_2 observed in the LIG with a larger linewidth could be explained by the limited recovery at a lower temperature (Fig. 4c and d) at the edge region from the non-uniform temperature distribution as well.

After uncovering the width effect, we further investigated the temperature effect on the gas sensor performance. By leveraging the self-heating effect in the LIG sensing region, the gas sensing behaviours of the rGO/MoS_2-LIG sensor to NO_2 of 1 ppm were compared at various operating temperatures from 20 °C to 80 °C (Fig. 4c and d). The operating temperature was selected to be below 100 °C because of the stability consideration of the ion-osorption of gas species in the charge transfer involving MoS_2.[68] While a complete recovery was observed in the LIG gas sensing platform with rGO/MoS_2 nanoflowers of the small petal structure, the recovery time of 2830 s to 1 pm NO_2 at 20 °C was significantly larger than that at 80 °C (580 s) (Fig. S9†). Also, it is crucial to sensitively detect low concentrations of NO_2 (~53 ppb) in the envisioned applications, as this level of exposure can cause chronic bronchitis, emphysema, and respiratory irritation.[30] The repeatability test indicates that the response of the gas sensor to the same target gas concentration is independent of whether the gas sensor is fully recovered. Thus, the gas sensor does not necessarily need to fully recover when used for the long-term monitoring of low-level exposures. Considering a recovery time of 720 s is sufficient to capture the gas sensor characteristics, this value is used in the subsequent tests for rapid testing (as in literature studies) unless otherwise specified. As the operating temperature was increased from 20 °C to 80 °C, the response of the sensor with the big petal structure gradually decreased from 2.8‰ to 0.4‰ upon exposure to NO_2 for 6 min (Fig. 4c). As the maximum response is often observed at optimum operating temperature for many low-dimensional and metal oxide nanomaterials, the reduced response at the elevated temperature is consistent with the previous study on MoS_2/graphene hybrid structure.[30] While the temperature-dependent response is related to the equilibrium of the NO_2 adsorption, further experiments are still needed to directly uncover the underlying mechanism. However, the elevated operating temperature led to improvements in the response/recovery processes of the gas sensor. The decreased slope of the plateau from 11° to 0.7° indicated the significantly improved response process (Fig. S10a†). Defining the recovery ratio as the ratio of responses at the end to the start of desorption in given time duration, the recovery rate also increased from 20% to 200% for desorption of 12 min as the operating temperature was increased from 20 °C to 80 °C. The improved desorption was enabled by thermal activation at elevated operating temperatures.[30]

A balance has to be struck as the significant response and fast response/recovery cannot be achieved simultaneously by tuning the operating temperature alone. This observation also held for the LIG with the small petal structure. While the response of the sensor decreased from 6.6‰ to 2.0‰ as the operating temperature was increased from 20 °C to 80 °C, the angle of plateau decreased from 8° to 0.6° (Fig. S10b†), and the recovery rate increased from 58% to 113% (Fig. 4d). Considering the balance between the significant response and fast response/recovery processes, the operating temperature of 60 °C was selected in the subsequent studies unless specified otherwise. The room or low temperature sensing capability was particularly attractive for wearable gas sensing applications due to low energy consumption and the elimination of the adverse thermal effect on the skin surface. Though the operating temperature of 60 °C seems to be slightly higher than the desired temperature in the epidermal applications, incorporating a heat sink or combining the thermal isolation layer in the gas sensor could readily reduce the temperature at the sensor/skin interface to avoid the adverse thermal effect on the skin surface.

In the typical dynamic response test, the rGO/MoS_2-LIG sensor showed a response of 1.80‰, 2.90‰, 3.96‰, 4.70‰, 5.30‰, 7.60‰, and 9.50‰ as the concentration of NO_2 was progressively ramped up from 0.2 to 0.4, 0.6, 0.8, 1.0, 2.0, and 5.0 ppm, respectively (Fig. 5a). The monotonically reversible sensing result demonstrated a relatively wide detection range for NO_2 to meet the requirements of air quality monitoring and exhaled breath detecting.[10] Exposing the gas sensor to NO_2 of 1 ppm for five consecutive cycles also indicated excellent repeatability, with a relatively stable response of 5‰ and fast response/recovery processes of 360 s/720 s (Fig. 5b). Additionally, the stable response of 5‰ was observed regardless of the incomplete recovery, indicating the full recovery is not necessarily needed for the envisioned applications of long-term monitoring of low-level exposures.

In addition to the response and response/recovery processes, the signal-to-noise ratio (SNR) is another critical parameter in the performance assessment of gas sensors, especially relevant to the calculation of the limit of detection (LOD). In spite of the relatively small responses of a few ‰, the SNR of the rGO/MoS_2-LIG with the small (or big) petal structure to 1 ppm NO_2 gas was 269/482/213/339 (or 331/421/530/132) at 20/40/60/80 °C (Fig. S11†), which is significantly higher than most of the values in the previous reports based on 2D material.[64] The highly porous LIG and the rGO/MoS_2 nanoflowers with a high specific area resulted in low contact resistance, thereby leading to low noise and high SNR.

One parameter to represent the level of noise is its standard deviation RMS_{noise} in the baseline of the response curve. Calculating the RMS_{noise} value from 100 data points in the response curves (Fig. S12†) of the rGO/MoS_2-LIG sensor with the small (or big) petal structure to NO_2 in the concentration range from 200 ppb to 600 ppb yielded 0.0030‰ (or 0.0036‰). The slope of the simple linear fit in the linear calibration curves (*i.e.*, between the response and NO_2 concentration) was obtained to be 7.49‰ ppm^{-1} (or 5.42‰ ppm^{-1}) for the one with the small

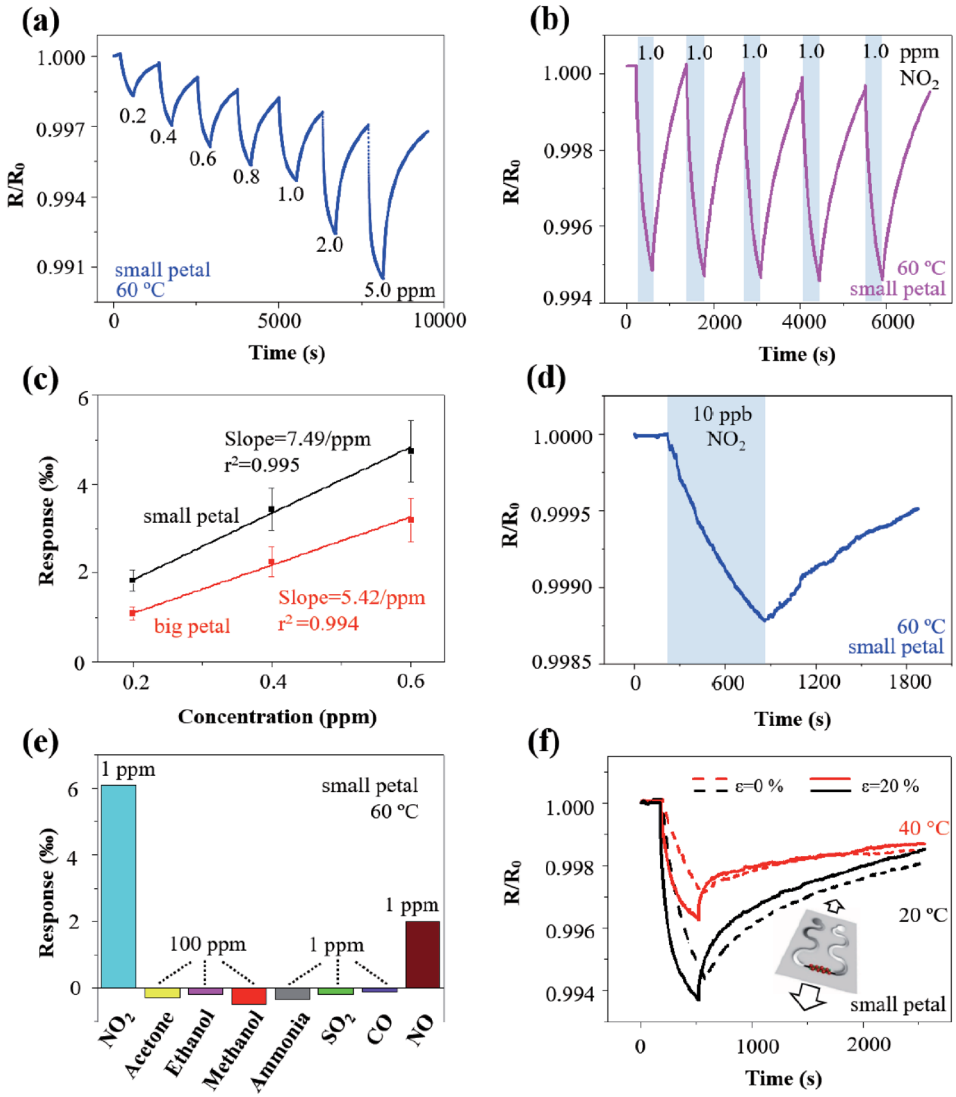

Fig. 5 The dynamic response, limit of detection, selectivity, and mechanical robustness of the gas sensor. (a) Dynamic response test of the gas sensor with the small petal structure in the presence of NO_2 from 0.2 ppm to 5 ppm at 60 °C from self-heating (applied voltage of 10 V). (b) Demonstration of repeatability to NO_2 of 1 ppm for five consecutive cycles. (c) A linear fit to the calibration curves obtained from the sensor response to NO_2 of 200 ppb, 400 ppb, and 600 ppb at 60 °C from self-heating. (d) Experimental demonstration of the ultralow limit of detection to NO_2 of 10 ppb at 60 °C, where a high signal-to-noise ratio (SNR) of 62 was still measured. (e) The selectivity of the stretchable rGO/MoS_2-LIG gas sensor to NO_2 over a wide range of other inferencing gaseous molecules at 60 °C before stretching. (f) Response of the stretchable gas sensor in (e) to NO_2 of 1 ppm before and after a uniaxial tensile strain of 20% was applied at room temperature and 40 °C, respectively (ppb: parts per billion; 1 ppb = 10^{-7}%).

(or big) petal structure (Fig. 5c). Defining the LOD as 3 × RMS_{noise}/slope,[69] the theoretical estimation of the LOD could be extrapolated from the above linear calibration curves and calculated to be 1.2 ppb (or 2.0 ppb) for the sensor with the small (or big) petal structure. In the validation experiment, an SNR of 62 was still measured with fast response and nearly complete recovery in the sensor with the small petal structure in the presence of 10 ppb NO_2 (Fig. 5d). Because the LOD could also be interpreted as the concentration with a signal to be approximately three times of the noise, the measured SNR of 62 in Fig. 5d indicated an actual LOD of less than 1 ppb into the parts per trillion (ppt) range. Though this actual LOD is challenging to be validated with our current static gas testing setup, it will be demonstrated with a more precise testing setup in future studies. The NO_2 gas sensors with an ultralow LOD and self-heating capabilities demonstrated with a simple fabrication method in this study compared favourably to previous studies based on low-dimensional nanomaterials (Table 1).

The selectivity of the rGO/MoS_2-LIG sensor to NO_2 was confirmed in comparison to the responses to a wide range of other interfering gas species that include acetone, ethanol, methanol, ammonia, SO_2, CO, and NO (Fig. 5e). While the sensor response to NO_2 of 1 ppm was 5.1‰, its response was only −0.34‰ to ammonia (NH_3) of 1 ppm, 2.0/−0.19/−0.11‰ to NO/SO_2/CO of 1 ppm, and −0.3/−0.19/−0.5‰ to acetone/ethanol/methanol (CH_3COCH_3/C_2H_5OH/CH_3OH) of 100 ppm.

Table 1 Comparison between LIG-based gas sensors and recently published NO_2 gas sensors

Materials	Temperature	Response/recovery time (s)	LOD (ppb)	Electrode fabrication	Heater	Flexible or stretchable	Reference
MoS_2/graphene	200	21.6/29.4 (0.5 ppm)	14	Pt/Ti electrodes (deposition)	Micro-heater	No	Long 2016 (ref. 30)
rGO/MoS_2	60	—	5.7	Au/Ti-IDE (lithography, sputter)	External heater	No	Zhou 2017 (ref. 31)
Single-layer MoS_2	200	660/720 (1 ppm)	20	rGO electrodes (spin coat, hydrazine vapor)	External heater	No	Donarelli 2015 (ref. 70)
Single-layer graphene	250	26/480 (40 ppm)	500	Cr/Au (single deposition)	Flexible and transparent heater	Bendable, but not stretchable	Choi 2014 (ref. 26)
Single-layer MoS_2	RT	800/1000 (25 ppb)	0.1	Au/Gr electrodes (photolithography, electron-beam metal deposition)	N/A	No	Pham 2019 (ref. 71)
MoS_2/SiO_2	100	1500/2500 (50 ppm)	8.84	Pt-IDE	External heater	No	Shim 2018 (ref. 68)
MoS_2–MoO_3 microflowers	RT	15/182 (10 ppm)	—	Au/Cr (shadow mask deposition)	N/A	No	Kumar 2018 (ref. 72)
Atomic-layered MoS_2	RT/100	120/1680 (1.2 ppm)	120	Au/Cr-IDE (deposition)	External heater	No	Cho 2015 (ref. 34)
3D MoS_2 aerogel	200	33/107 (0.5 ppm)	28	Pt/Ti electrodes (deposition)	Poly-silicon heater	No	Long 2017 (ref. 73)
Vertical MoS_2	RT	—	100	Pt/Ti electrodes (deposition)	N/A	No	Kumar 2018 (ref. 74)
Mixed MoS_2 flakes	125	4.4/19.6 (10 ppm)	—	—	—	No	Agrawal 2018 (ref. 75)
MoS_2/SnO_2	RT	408/162 (0.5 ppm)	500	Au (deposition)	N/A	No	Cui 2015 (ref. 76)
SnS_2	120	170/140 (5 ppm)	20–30	Pt-IDE electrodes (deposition)	External heater	No	Ou 2015 (ref. 9)
Black phosphorus (BP)	RT	5/not recover (100 ppm)	100	Au (deposition)	N/A	No	Cho 2016 (ref. 77)
Ag-WS_2	100	300/600 (25 ppm)	—	Au/Cr electrodes (deposition)	—	No	Ko 2016 (ref. 78)
$MoSe_2$ nanosheets	RT	250/150 (1 ppm)	10	Au electrodes (deposition)	NA	Stretchable	Guo 2019 (ref. 79)
Reduced graphene/ZnO	150	28/— (100 ppm)	1000	Au/Cr-IDE electrodes (shadow mask deposition)	External heater	No	Bhati 2018 (ref. 80)
Graphene	RT	—	650	Pt/Ti-IDE (photolithography, deposition)	N/A	No	Choi 2015 (ref. 81)
rGO/MoS_2-LIG, small (or big) petal	60	360/720 (1 ppm)	1.2 (or 2.0)	LIG electrodes (laser scribing + metal coating)	Self-heating	Stretchable (tensile strain of 20%)	This work

Though the concentration of the volatile organic compounds (VOCs) was much higher than that of NO_2, the sensor response was still much smaller because of their weak interaction with the gas sensing nanomaterials. The sensor responses to NH_3/SO_2/CO of 1 ppm were small yet considerable, but they were in the opposite direction because of their reducing characteristics.[82,83] In addition to the common interfering gas species such as NH_3, NO, CO, SO_2, and VOCs in the target application environment, humidity often poses significant concern on the gas sensors, especially for those operating at room or low temperatures. Exposing the gas sensor at a high level of relative humidity (RH) demonstrated the humidity effect. After being exposed to an RH of 88% for 6 min, the humidity response was considerable at 20 °C (*i.e.*, 1.96‰). However, the response was significantly reduced at elevated temperatures (*i.e.*, 0.83/0.45/0.29‰ at 40/60/80 °C) (Fig. S13†), indicating a small interfering effect of RH on NO_2 response at elevated temperatures. Coating metal–organic framework (MOF) such as a layer of hydrophobic and catalytic Zeolitic Imidazolate Framework-CoZn (ZIF-CoZn, isostructural with ZIF-8(Zn) or ZIF-67(Co)) thin film on the gas sensor could also drastically improve the sensor performance under humidity interference.[84] Additionally, the concept from the electronic nose could be applied to deconvolute the gas response in the presence of humidity based on the measurements from two sensors with one subject to both gas and humidity and the other one subject to humidity alone.[85]

When used in epidermal applications, the LIG gas sensing platform also expects to be mechanically robust with minimum resistance change upon mechanical perturbations such as natural skin motions. As stretchable structures have been extensively studied and explored to ensure stretchable properties in the epidermal devices, they will be exploited to yield a stretchable LIG gas sensing platform. Leveraging the simple laser scribing process, the stretchable serpentine interconnect region can be created during the sensor fabrication in a single step. Because of the serpentine interconnect region, the rGO/MoS_2-LIG gas sensor on an elastomeric substrate such as Ecoflex exhibited a robust mechanical property (Fig. 5f) to withstand a uniaxial tensile strain ε of 20% that is comparable to the level of the maximum deformation on the skin surface.[86] The mechano-chemiresistive properties of the rGO/MoS_2-LIG gas sensor with the small petal structure to NO_2 of 1 ppm were investigated. The static tensile strain was applied from a custom-built stretcher with a step motor controlled by Arduino Uno, and the gas sensor was evaluated at both room temperature and 40 °C from self-heating. In addition to maintaining its mechanical integrity, the sensor subject to a uniaxial tensile strain of 20% demonstrated an increased response and faster recovery when compared to the un-stretched (*i.e.*, $\varepsilon = 0\%$) at both room temperature and 40 °C. As the tensile strain was increased from 0% to 20%, the sensor response increased from 5.5‰ to 6.2‰ (or from 2.8‰ to 4.0‰) at 20 °C (or 40 °C). The increased response and faster recovery upon mechanical deformation could be attributed to the deformation-induced structure change in the highly porous LIG and the strain engineering of the semiconducting nanomaterials. As a simple and straightforward strategy, strain isolation with a stiff material in the sensing region was explored to demonstrate ways to reduce the strain interfering. A tensile strain of 20% was applied from a custom-built stretcher on the LIG gas sensing platform with three different strain isolation designs (Fig. S14a†). As the existing PI beneath the LIG has Young's modulus much larger than that of the elastomeric substrate, it naturally served as the stiff material for strain isolation. Because of the enhanced stiffness in the device region and the placement of the LIG sensor away from the strain concentration edge,[87–89] the strain in the LIG sensor is significantly reduced when compared to the applied strain. Progressively increasing the size of the PI pattern (*i.e.*, single line, small circle, and large circle) enhanced the strain isolation effect by moving the LIG gas sensor away from the strain concentration edge. As a result, the resistance change in the LIG gas sensing platform reduced from 11.3‰ for the single line design to 0.47‰ for the large circle design, when a strain of 20% was applied perpendicular to the sensing region. The resistance fluctuation was also greatly suppressed for the large circle design compared with the other two designs (Fig. S14c and d†). While the LIG gas sensing platform could be attached to the skin surface with its sensing line perpendicular to the major deformation direction, the strain along the parallel direction of the sensing line may not be ignored. In the LIG gas sensing array, the spacing between two sensors could actually follow most of the strain applied to the array with different strain isolation designs. When a strain of 20% parallel to the LIG sensing line was applied, the resistance change in the LIG gas sensing platform reduced from 77.8‰ for the single line design to 4.4‰ for the large circle design. Replacing the spacing with a much compliant material would certainly improve the strain isolation effect to result in a much smaller resistance change. Other than the demonstrated strain isolation strategy, many other stretchable strategies (*e.g.*, pre-strain,[90] self-similar interconnect patterns,[91] and kirigami patterning of the substrate[92]) can also be applied to further minimize the strain and reduce the resistance change in the LIG sensing region. While the strain-induced resistance change cannot be ignored for the detection of the ultralow concentration of NO_2, the concept from the electronic nose to deconvolute the gas response in the presence of strain can also be applied here, similar to the proposed strategy to mitigate the humidity effect. The demonstrated stretchable gas sensors could enable the conformal contact to the hierarchically textured skin surface for applications in epidermal electronic devices.

The deconvolution of multiple gaseous components from a mixture requires the use of a high-density gas sensor array with each of the different selectivity. As the first step to demonstrate such a capability of the LIG gas sensing platform, we will demonstrate the application of the LIG gas sensing platform goes from characterization of low-dimensional nanomaterials to a different class of nanomaterials such as heterostructure metal oxides. As a representative heterostructure metal oxide, ZnO/CuO core/shell nanomaterials were first prepared by calcination of a Cu–Zn bimetallic metal–organic framework (MOF) (Fig. S15†). Dispersing the ZnO/CuO core/shell nanomaterials in the LIG sensing regions (power of 16%, speed of 10% in the laser scribing process) in a different sensing

unit in the array yielded a gas sensor with a response of 1.5‰ and an SNR 390 of to NO_2 of 1 ppm (Fig. S16a†). In contrast to the sensing unit with rGO/MoS_2 (or MoS_2), the sensing unit with ZnO/CuO core/shell nanomaterials exhibited a different selectivity with significant responses to VOCs (Fig. S16b†). Considering the other nanomaterials with a different selectivity to VOCs (*e.g.*, ZnO based ammonia gas sensor[93,94]), an array of sensing units with different selectivity to the gaseous components in the mixture could be prepared. As different selectivity in various sensing units of the array is required to detect gaseous components from a mixture based on the algorithm from the electronic nose, the result from this study also paves the ways for applying the novel LIG gas sensing platform in an array layout to the electronic nose.

Conclusions

In summary, we have developed a novel gas sensing platform based on porous laser-induced graphene (LIG) with a metal surface coating. Consisting of an LIG sensing region and an Ag/LIG serpentine interconnect region, the LIG gas sensing platform as a chemiresistor provides an alternative to interdigitated electrodes with separate heaters for integrating and characterizing the performance of gas-sensitive nanomaterials. The metal surface coating on the LIG in the interconnect region has induced location-dependent conductivity to significantly reduce its resistance, which enables highly localized Joule heating (*i.e.*, self-heating) during the measurement of the chemiresistor. The fast (to reach equilibrium within 20 s) and well-controlled (by externally applied voltage) self-heating capability in the LIG gas sensing platform eliminates the need for a separate heating element, which significantly reduces the fabrication complexity. As one demonstration to show the capabilities of this new gas sensing platform, highly sensitive nanomaterials such as MoS_2 and rGO/MoS_2 have been dispersed on the LIG sensing region to result in an ultrasensitive chemiresistive NO_2 gas sensor. Due to the large specific surface area in the nanomaterials and highly porous LIG, rich yet specific active sites in the MoS_2, and possible formation of p–n heterojunctions in rGO/MoS_2, the resulting gas sensor exhibits relatively large response, fast response/recovery processes, and excellent selectivity at slightly elevated temperature from self-heating in a static testing setup. The drastically reduced noise levels resulted in a significantly increased SNR (*e.g.*, close to 900 to NO_2 of 1 ppm), which enables the sensor to detect NO_2 at a concentration of a few ppb. Based on the experimental demonstration, the actual limit of detection is believed to be smaller than 1 ppb. The effects of the LIG sensing region geometric parameters, operating temperature, and various nanomaterials on the gas sensing performance have also been systematically investigated. Configuring the serpentine interconnect region in a stretchable layout, the resulting LIG gas sensing platform becomes mechanically robust even under a uniaxial tensile strain of 20% that is comparable to the maximum deformation on the skin surface. Considering the other stretchable strategies, the strain interfering could be further minimized. When incorporating a heat sink or combining the thermal isolation layer in the gas sensor to avoid the adverse thermal effect on the skin surface, the novel LIG gas sensing platform that could deconvolute multiple gaseous components in a mixture opens new opportunities for the epidermal electronic devices.

Conflicts of interest

The authors declare no conflicts of interest.

Acknowledgements

The manuscript was written through the contributions of all authors. All authors have approved the final version of the manuscript. Acknowledgment is made to the start-up fund at The Pennsylvania State University, National Science Foundation (NSF) (Grant No. ECCS-1933072), and the start-up grant and Tier1 fund to H. Z. from Northeastern University for support of this research. The partial support from the Materials for Enhancing Energy and Environmental Stewardship Seed Grant Program and the Commonwealth Campuses & Shared Facilities & Collaboration Development Program at Penn State, the State Key Laboratory of Digital Manufacturing Equipment and Technology at Huazhong University of Science and Technology (Grant no. DMETKF2019004), and NSFC (Grant No. 11572161 and 51705126) is also acknowledged. The help of LIG fabrication from Mr Zhendong Liu and stretchability test from Mr Zhaozheng Yu is acknowledged. One or more provisional patents are being filed on this work.

Notes and references

1 J. Shi, X. Li, H. Cheng, Z. Liu, L. Zhao, T. Yang, Z. Dai, Z. Cheng, E. Shi and L. Yang, *Adv. Funct. Mater.*, 2016, **26**, 2078–2084.
2 J. Yang, D. Wei, L. Tang, X. Song, W. Luo, J. Chu, T. Gao, H. Shi and C. Du, *RSC Adv.*, 2015, **5**, 25609–25615.
3 W. Gao, S. Emaminejad, H. Y. Y. Nyein, S. Challa, K. Chen, A. Peck, H. M. Fahad, H. Ota, H. Shiraki and D. Kiriya, *Nature*, 2016, **529**, 509.
4 W. H. Yeo, Y. S. Kim, J. Lee, A. Ameen, L. Shi, M. Li, S. Wang, R. Ma, S. H. Jin and Z. Kang, *Adv. Mater.*, 2013, **25**, 2773–2778.
5 A. Tricoli, N. Nasiri and S. De, *Adv. Funct. Mater.*, 2017, **27**, 1605271.
6 E. Singh, M. Meyyappan and H. S. Nalwa, *ACS Appl. Mater. Interfaces*, 2017, **9**, 34544–34586.
7 Y. Yang and Z. D. Deng, *Appl. Phys. Rev.*, 2019, **6**, 011309.
8 W. Li, C. Teng, Y. Sun, L. Cai, J.-L. Xu, M. Sun, X. Li, X. Yang, L. Xiang and D. Xie, *ACS Appl. Mater. Interfaces*, 2018, **10**, 34485–34493.
9 J. Z. Ou, W. Ge, B. Carey, T. Daeneke, A. Rotbart, W. Shan, Y. Wang, Z. Fu, A. F. Chrimes and W. Wlodarski, *ACS Nano*, 2015, **9**, 10313–10323.
10 H. Khan, A. Zavabeti, Y. Wang, C. J. Harrison, B. J. Carey, M. Mohiuddin, A. F. Chrimes, I. A. De Castro, B. Y. Zhang and Y. M. Sabri, *Nanoscale*, 2017, **9**, 19162–19175.

11 G. Hoek, R. M. Krishnan, R. Beelen, A. Peters, B. Ostro, B. Brunekreef and J. D. Kaufman, *Environ. Health*, 2013, **12**, 43.
12 M.-W. Ahn, K.-S. Park, J.-H. Heo, J.-G. Park, D.-W. Kim, K. J. Choi, J.-H. Lee and S.-H. Hong, *Appl. Phys. Lett.*, 2008, **93**, 263103.
13 A. Forleo, L. Francioso, S. Capone, P. Siciliano, P. Lommens and Z. Hens, *Sens. Actuators, B*, 2010, **146**, 111–115.
14 T. Wang, D. Huang, Z. Yang, S. Xu, G. He, X. Li, N. Hu, G. Yin, D. He and L. Zhang, *Nano-Micro Lett.*, 2016, **8**, 95–119.
15 Z. Chen, J. Wang, A. Umar, Y. Wang, H. Li and G. Zhou, *ACS Appl. Mater. Interfaces*, 2017, **9**, 11819–11827.
16 F. Schedin, A. Geim, S. Morozov, E. Hill, P. Blake, M. Katsnelson and K. Novoselov, *Nat. Mater.*, 2007, **6**, 652.
17 W. Li, X. Geng, Y. Guo, J. Rong, Y. Gong, L. Wu, X. Zhang, P. Li, J. Xu and G. Cheng, *ACS Nano*, 2011, **5**, 6955–6961.
18 G. Jiang, M. Goledzinowski, F. J. Comeau, H. Zarrin, G. Lui, J. Lenos, A. Veileux, G. Liu, J. Zhang and S. Hemmati, *Adv. Funct. Mater.*, 2016, **26**, 1729–1736.
19 S. Wan, J. Peng, L. Jiang and Q. Cheng, *Adv. Mater.*, 2016, **28**, 7862–7898.
20 L. Banszerus, M. Schmitz, S. Engels, J. Dauber, M. Oellers, F. Haupt, K. Watanabe, T. Taniguchi, B. Beschoten and C. Stampfer, *Sci. Adv.*, 2015, **1**, e1500222.
21 X. Tang, A. Du and L. Kou, *Wiley Interdiscip. Rev.: Comput. Mol. Sci.*, 2018, **8**, e1361.
22 Y. Li, Z. Peng, E. Larios, G. Wang, J. Lin, Z. Yan, F. Ruiz-Zepeda, M. José-Yacamán and J. M. Tour, *ACS Nano*, 2014, **9**, 532–538.
23 Y. Wang, J. Chen and X. Huang, *Phys. Status Solidi C*, 2017, **14**, 1600110.
24 W. Yuan, A. Liu, L. Huang, C. Li and G. Shi, *Adv. Mater.*, 2013, **25**, 766–771.
25 J. D. Fowler, M. J. Allen, V. C. Tung, Y. Yang, R. B. Kaner and B. H. Weiller, *ACS Nano*, 2009, **3**, 301–306.
26 H. Choi, J. S. Choi, J. S. Kim, J. H. Choe, K. H. Chung, J. W. Shin, J. T. Kim, D. H. Youn, K. C. Kim and J. I. Lee, *Small*, 2014, **10**, 3685–3691.
27 H.-P. Komsa, J. Kotakoski, S. Kurasch, O. Lehtinen, U. Kaiser and A. V. Krasheninnikov, *Phys. Rev. Lett.*, 2012, **109**, 035503.
28 Q. Yue, S. Chang, S. Qin and J. Li, *Phys. Lett. A*, 2013, **377**, 1362–1367.
29 K. Dolui, I. Rungger, C. D. Pemmaraju and S. Sanvito, *Phys. Rev. B: Condens. Matter Mater. Phys.*, 2013, **88**, 075420.
30 H. Long, A. Harley-Trochimczyk, T. Pham, Z. Tang, T. Shi, A. Zettl, C. Carraro, M. A. Worsley and R. Maboudian, *Adv. Funct. Mater.*, 2016, **26**, 5158–5165.
31 Y. Zhou, G. Liu, X. Zhu and Y. Guo, *Sens. Actuators, B*, 2017, **251**, 280–290.
32 K. Lee, R. Gatensby, N. McEvoy, T. Hallam and G. S. Duesberg, *Adv. Mater.*, 2013, **25**, 6699–6702.
33 B. Cho, M. G. Hahm, M. Choi, J. Yoon, A. R. Kim, Y.-J. Lee, S.-G. Park, J.-D. Kwon, C. S. Kim and M. Song, *Sci. Rep.*, 2015, **5**, 8052.
34 B. Cho, A. R. Kim, Y. Park, J. Yoon, Y.-J. Lee, S. Lee, T. J. Yoo, C. G. Kang, B. H. Lee and H. C. Ko, *ACS Appl. Mater. Interfaces*, 2015, **7**, 2952–2959.
35 J. Courbat, D. Briand and N. F. de Rooij, *Sens. Actuators, A*, 2008, **142**, 284–291.
36 I. Simon, N. Bârsan, M. Bauer and U. Weimar, *Sens. Actuators, B*, 2001, **73**, 1–26.
37 J. N. Calata, G.-Q. Lu, K. Ngo and L. Nguyen, *J. Electron. Mater.*, 2014, **43**, 109–116.
38 M. Bobinger, D. Angeli, S. Colasanti, P. La Torraca, L. Larcher and P. Lugli, *Phys. Status Solidi A*, 2017, **214**, 1600466.
39 M. Bobinger, J. Mock, P. La Torraca, M. Becherer, P. Lugli and L. Larcher, *Adv. Mater. Interfaces*, 2017, **4**, 1700568.
40 M. Camara, P. Breuil, C. Pijolat, J.-P. Viricelle, N. F. de Rooij and D. Briand, *Sens. Actuators, B*, 2016, **236**, 1111–1117.
41 G. Lu, S. Park, K. Yu, R. S. Ruoff, L. E. Ocola, D. Rosenmann and J. Chen, *ACS Nano*, 2011, **5**, 1154–1164.
42 M. Qazi, T. Vogt and G. Koley, *Appl. Phys. Lett.*, 2007, **91**, 233101.
43 R. Arsat, M. Breedon, M. Shafiei, P. Spizziri, S. Gilje, R. Kaner, K. Kalantar-zadeh and W. Wlodarski, *Chem. Phys. Lett.*, 2009, **467**, 344–347.
44 S.-J. Choi and I.-D. Kim, *Electron. Mater. Lett.*, 2018, **14**, 221–260.
45 J. Lin, Z. Peng, Y. Liu, F. Ruiz-Zepeda, R. Ye, E. L. Samuel, M. J. Yacaman, B. I. Yakobson and J. M. Tour, *Nat. Commun.*, 2014, **5**, 5714.
46 R. Ye, Z. Peng, T. Wang, Y. Xu, J. Zhang, Y. Li, L. G. Nilewski, J. Lin and J. M. Tour, *ACS Nano*, 2015, **9**, 9244–9251.
47 M. Smith, D. Luong, T. Bougher, K. Kalaitzidou, J. Tour and B. Cola, *Appl. Phys. Lett.*, 2016, **109**, 253107.
48 N. T. Garland, E. S. McLamore, N. D. Cavallaro, D. Mendivelso-Perez, E. A. Smith, D. Jing and J. C. Claussen, *ACS Appl. Mater. Interfaces*, 2018, **10**, 39124–39133.
49 B. Sun, R. N. McCay, S. Goswami, Y. Xu, C. Zhang, Y. Ling, J. Lin and Z. Yan, *Adv. Mater.*, 2018, **30**, 1804327.
50 X. Zang, C. Shen, Y. Chu, B. Li, M. Wei, J. Zhong, M. Sanghadasa and L. Lin, *Adv. Mater.*, 2018, **30**, 1800062.
51 C. Zhang, Y. Xie, C. Zhang and J. Lin, *Carbon*, 2019, **153**, 585–591.
52 M. Dosi, I. Lau, Y. Zhuang, D. S. Simakov, M. W. Fowler and M. A. Pope, *ACS Appl. Mater. Interfaces*, 2019, **11**, 6166–6173.
53 M. G. Stanford, K. Yang, Y. Chyan, C. Kittrell and J. M. Tour, *ACS Nano*, 2019, **13**, 3474–3482.
54 D. Wu, Q. Peng, S. Wu, G. Wang, L. Deng, H. Tai, L. Wang, Y. Yang, L. Dong and Y. Zhao, *Sensors*, 2018, **18**, 4405.
55 M. R. Bobinger, F. J. Romero, A. Salinas-Castillo, M. Becherer, P. Lugli, D. P. Morales, N. Rodríguez and A. Rivadeneyra, *Carbon*, 2019, **144**, 116–126.
56 A. C. Ferrari, J. Meyer, V. Scardaci, C. Casiraghi, M. Lazzeri, F. Mauri, S. Piscanec, D. Jiang, K. Novoselov and S. Roth, *Phys. Rev. Lett.*, 2006, **97**, 187401.
57 Q. He, Z. Zeng, Z. Yin, H. Li, S. Wu, X. Huang and H. Zhang, *Small*, 2012, **8**, 2994–2999.
58 Y. C. Kim, V. T. Nguyen, S. Lee, J.-Y. Park and Y. H. Ahn, *ACS Appl. Mater. Interfaces*, 2018, **10**, 5771–5778.

59 W.-J. Su, H.-C. Chang, Y.-T. Shih, Y.-P. Wang, H.-P. Hsu, Y.-S. Huang and K.-Y. Lee, *J. Alloys Compd.*, 2016, **671**, 276–282.
60 L. Chen, X. Geng, L. Yang, W. Liang and H. Zhu, *Int. J. Hydrogen Energy*, 2017, **42**, 26659–26666.
61 X. Liu, Z. Xing, Y. Zhang, Z. Li, X. Wu, S. Tan, X. Yu, Q. Zhu and W. Zhou, *Appl. Catal., B*, 2017, **201**, 119–127.
62 S. Ji, W. He, K. Wang, Y. Ran and C. Ye, *Small*, 2014, **10**, 4951–4960.
63 J. Kang, H. Kim, K. S. Kim, S.-K. Lee, S. Bae, J.-H. Ahn, Y.-J. Kim, J.-B. Choi and B. H. Hong, *Nano Lett.*, 2011, **11**, 5154–5158.
64 Y. H. Yoon, J. W. Song, D. Kim, J. Kim, J. K. Park, S. K. Oh and C. S. Han, *Adv. Mater.*, 2007, **19**, 4284–4287.
65 A. A. Balandin, *Nat. Mater.*, 2011, **10**, 569.
66 S. J. Kim, H.-J. Koh, C. E. Ren, O. Kwon, K. Maleski, S.-Y. Cho, B. Anasori, C.-K. Kim, Y.-K. Choi and J. Kim, *ACS Nano*, 2018, **12**, 986–993.
67 S. Yu, S. Wang, M. Lu and L. Zuo, *Sens. Actuators, A*, 2017, **257**, 58–64.
68 Y.-S. Shim, K. C. Kwon, J. M. Suh, K. S. Choi, Y. G. Song, W. Sohn, S. Choi, K. Hong, J.-M. Jeon and S.-P. Hong, *ACS Appl. Mater. Interfaces*, 2018, **10**, 31594–31602.
69 L. A. Currie, *Pure Appl. Chem.*, 1995, **67**, 1699–1723.
70 M. Donarelli, S. Prezioso, F. Perrozzi, F. Bisti, M. Nardone, L. Giancaterini, C. Cantalini and L. Ottaviano, *Sens. Actuators, B*, 2015, **207**, 602–613.
71 T. Pham, G. Li, E. Bekyarova, M. E. Itkis and A. Mulchandani, *ACS Nano*, 2019, 3196–3205.
72 R. Kumar, N. Goel, M. Mishra, G. Gupta, M. Fanetti, M. Valant and M. Kumar, *Adv. Mater. Interfaces*, 2018, **5**, 1800071.
73 H. Long, L. Chan, A. Harley-Trochimczyk, L. E. Luna, Z. Tang, T. Shi, A. Zettl, C. Carraro, M. A. Worsley and R. Maboudian, *Adv. Mater. Interfaces*, 2017, **4**, 1700217.
74 R. Kumar, P. K. Kulriya, M. Mishra, F. Singh, G. Gupta and M. Kumar, *Nanotechnology*, 2018, **29**, 464001.
75 A. V. Agrawal, R. Kumar, S. Venkatesan, A. Zakhidov, G. Yang, J. Bao, M. Kumar and M. Kumar, *ACS Sens.*, 2018, **3**, 998–1004.
76 S. Cui, Z. Wen, X. Huang, J. Chang and J. Chen, *Small*, 2015, **11**, 2305–2313.
77 S. Y. Cho, Y. Lee, H. J. Koh, H. Jung, J. S. Kim, H. W. Yoo, J. Kim and H. T. Jung, *Adv. Mater.*, 2016, **28**, 7020–7028.
78 K. Y. Ko, J.-G. Song, Y. Kim, T. Choi, S. Shin, C. W. Lee, K. Lee, J. Koo, H. Lee and J. Kim, *ACS Nano*, 2016, **10**, 9287–9296.
79 S. Guo, D. Yang, S. Zhang, Q. Dong, B. Li, N. Tran, Z. Li, Y. Xiong and M. E. Zaghloul, *Adv. Funct. Mater.*, 2019, **29**, 1900138.
80 V. S. Bhati, S. Ranwa, S. Rajamani, K. Kumari, R. Raliya, P. Biswas and M. Kumar, *ACS Appl. Mater. Interfaces*, 2018, **10**, 11116–11124.
81 Y. R. Choi, Y.-G. Yoon, K. S. Choi, J. H. Kang, Y.-S. Shim, Y. H. Kim, H. J. Chang, J.-H. Lee, C. R. Park and S. Y. Kim, *Carbon*, 2015, **91**, 178–187.
82 Y. H. Kim, S. J. Kim, Y.-J. Kim, Y.-S. Shim, S. Y. Kim, B. H. Hong and H. W. Jang, *ACS Nano*, 2015, **9**, 10453–10460.
83 Q. Yue, Z. Shao, S. Chang and J. Li, *Nanoscale Res. Lett.*, 2013, **8**, 425.
84 M. S. Yao, W. X. Tang, G. E. Wang, B. Nath and G. Xu, *Adv. Mater.*, 2016, **28**, 5229–5234.
85 W. Hu, L. Wan, Y. Jian, C. Ren, K. Jin, X. Su, X. Bai, H. Haick, M. Yao and W. Wu, *Adv. Mater. Technol.*, 2019, **4**, 1800488.
86 K.-I. Jang, H. U. Chung, S. Xu, C. H. Lee, H. Luan, J. Jeong, H. Cheng, G.-T. Kim, S. Y. Han and J. W. Lee, *Nat. Commun.*, 2015, **6**, 6566.
87 A. Romeo, Q. Liu, Z. Suo and S. P. Lacour, *Appl. Phys. Lett.*, 2013, **102**, 131904.
88 J. Lee, J. Wu, M. Shi, J. Yoon, S. I. Park, M. Li, Z. Liu, Y. Huang and J. A. Rogers, *Adv. Mater.*, 2011, **23**, 986–991.
89 Y. Liu, Z. Liu, B. Zhu, J. Yu, K. He, W. R. Leow, M. Wang, B. K. Chandran, D. Qi, H. Wang, G. Chen, C. Xu and X. Chen, *Adv. Mater.*, 2017, **29**, 1701780.
90 Y. Zhang, S. Wang, X. Li, J. A. Fan, S. Xu, Y. M. Song, K. J. Choi, W. H. Yeo, W. Lee and S. N. Nazaar, *Adv. Funct. Mater.*, 2014, **24**, 2028–2037.
91 S. Xu, Y. Zhang, J. Cho, J. Lee, X. Huang, L. Jia, J. A. Fan, Y. Su, J. Su and H. Zhang, *Nat. Commun.*, 2013, **4**, 1543.
92 Z. Wang, L. Zhang, S. Duan, H. Jiang, J. Shen and C. Li, *J. Mater. Chem. C*, 2017, **5**, 8714–8722.
93 M. Poloju, N. Jayababu and M. R. Reddy, *J. Mater. Sci. Eng. B*, 2018, **227**, 61–67.
94 M. Farbod, M. H. Joula and M. Vaezi, *Mater. Chem. Phys.*, 2016, **176**, 12–23.

